# Transport Upscaling in Highly Heterogeneous Aquifers and the Prediction of Tracer Dispersion at the MADE Site

Marco Dentz, Alessandro Comolli, Vivien Hakoun, Juan J. Hidalgo

# Transport upscaling in highly heterogeneous aquifers and the prediction of tracer dispersion at the Macrodispersion Experiment (MADE) site

Marco Dentz[1], Alessandro Comolli[1,2], Vivien Hakoun[1,3], and Juan Hidalgo[1]
[1] *Spanish National Research Council (IDAEA-CSIC), Barcelona, Spain**
[2] *Université Libre de Bruxelles (ULB), Nonlinear Physical Chemistry Unit, CP 231, 1050, Bruxelles, Belgium and*
[3] *BRGM, University of Montpellier, Montpellier, 34000, France*

We present an upscaled Lagrangian approach to predict the plume evolution in highly heterogeneous aquifers. The model is parameterized by transport independent characteristics such as the statistics of hydraulic conductivity and the Eulerian flow speed. It can be conditioned on the tracer properties, and flow data at the injection region. Thus, the model is transferable to different solutes and hydraulic conditions. It captures the large scale non-Gaussian features for the evolution of the longitudinal mass distribution observed for the bromide and tritium tracer plumes at the macrodispersion experiment (MADE) site (Columbus, Mississippi, USA), which are characterized by a slow moving peak and pronounced forward tailing. These large scale features are explained by advective tracer propagation due to a broad distribution of spatially persistent Eulerian flow speeds as a result of spatial variability in hydraulic conductivity.

## I. INTRODUCTION

The upscaling and prediction of tracer transport in highly heterogeneous porous and fractured media is of central concern in a broad range of subsurface applications from groundwater management to underground gas and waste storage. This task is challenging due to strong spatial variability in hydraulic conductivity values encountered in geological media [1].

Spatial variability in hydraulic conductivity induces spatial fluctuations in the flow and transport velocities, whose impact on large scale tracer migration has been quantified in terms of macrodispersion coefficients [2, 3]. For moderately heterogeneous media, Gelhar and Axness [2] used a stochastic modeling approach [4–6] to express the longitudinal macrodispersion coefficients in terms of the mean flow velocity, and the correlation length and variance of the logarithm of hydraulic conductivity. This expression is a central results for hydrogeological prediction because it allows to forecast macroscopic transport features based on transport independent observables.

However, spatial heterogeneity gives rise to transport behaviors that can be very different from the ones predicted by advection-dispersion models characterized by constant macrodispersion coefficients. For pointlike solute injections, the latter predicts Gaussian shaped tracer plumes and breakthrough curves, while observed distributions are typically found to be non-Gaussian [7–11]. This is the case for the tracer plumes monitored during the macrodispersion experiments conducted in the alluvial aquifer underlying the Columbus Air Force Base in northeastern Mississippi [7, 12]. Spatial tracer distributions are characterized by strongly non-Gaussian shapes characterized by a slowly moving peak and a pronounced forward tail. These and other observations of anomalous solute dispersion have spurred the development of non-Fickian transport theories [13–16]. Those include multirate mass transfer approaches [17, 18], continuous time random walks [13, 19], fractional advection-dispersion models [20, 21], time-domain random walks [22, 23], and space-time non-local advection-dispersion equations [24, 25]. While all of these approaches provide dynamic frameworks to model non-Gaussian large scale transport features, their parameterization in terms of transport independent parameters and thus their predictive power remain open questions.

The migration of the tracer plume at the MADE site was modeled by Berkowitz and Scher [26] with the continuous time random walk (CTRW) approach based on an empirical distribution of transition length and times, which reflects a broad distribution of mass transfer time scales. Benson *et al.* [27], Schumer *et al.* [28] and Zhang and Benson [29] modeled the tracer plumes of the MADE-1 experiment using a fractal mobile-immobile model that accounts for both solute retention due to a broad distribution of mass transfer time scale, and preferential transport due to a broad distribution of mass transfer length scales. The characteristic exponents of the model are estimated from the experimental data. Harvey and Gorelick [30] modeled the plume evolution using a multirate mass transfer (MRMT) model that considers rate limited mass transfer between a mobile domain with accelerating flow, and an immobile zone, which represents intragranular porosity, low permeability zones, dead end pores and surface sorption sites. These different processes are represented by a capacity coefficient, a rate coefficient, a retardation coefficient,

* E-mail: marco.dentz@csic.es

a velocity parameter and an acceleration parameter, which are estimated from the experimental mass data. These modeling approaches propose a range of mass transfer processes and invoke broad distributions of mass transfer time scales and lengths in order to simulate the impact of medium and flow heterogeneity on large scale transport. A key question in order to constrain such models refers to the dominant local scale mechanisms that cause non-Fickian large scale transport.

Mobile-immobile mass transfer has been studied as a mechanism to explain the decay of the apparent solute mass observed at the MADE-1 and MADE-2 experiments [30]. Feehley *et al.* [31] and Guan *et al.* [32] combine a stochastic reconstruction of aquifer heterogeneity based on fractal Brownian motion with mobile-immobile mass transfer in order to assess the plume evolution in the MADE-2 experiment. A series of works [33–35] have shown that a local scale advection-dispersion model based on the detailed knowledge of the spatial distribution of hydraulic conductivity allows reproducing the spatial distribution of tracer plumes observed at the MADE site. This implies that some key features of transport may indeed be understood from the spatial variability of hydraulic conductivity and thus advective heterogeneity. The question arising from this observation is whether characteristics of non-Fickian transport in strongly heterogeneous media can be predicted based only on a few geostatistical medium characteristics similar to the prediction of macrodispersion in moderately heterogeneous media. Along these lines, several authors [23, 36–38] investigated the relation between advective travel times and hydraulic conductivity, and the impact of broad distributions of the logarithm of hydraulic conductivity on non-Fickian transport. For example, the stochastic multi-indicator approach of Fiori *et al.* [23] was adapted in Fiori *et al.* [39] to predict the plume evolution of the MADE-1 experiment based on analytical expressions for the advective travel times over rectangular inclusions.

In this paper, we adress the questions of upscaling and prediction of dispersion in highly heterogeneous aquifers in terms of medium and flow heterogeneity, using transport independent parameters. We use a stochastic time domain random walk approach [40, 41] that accounts for heterogeneous advection. This approach propagates particles in space and time according to a velocity Markov model that is determined by the distribution of the Eulerian flow speed and correlation length. We discuss the model and its parameterization in terms of the medium and flow properties, and use it for the modeling and interpretation of the one-dimensional tracer profiles of the MADE-1 experiment.

## II. UPSCALED TRANSPORT MODEL

We employ the stochastic time-domain random walk (TDRW) implementation presented in [41] in order to build an upscaled model to predict the concentration evolution in highly heterogeneous aquifers, based on the statistical characteristics of the logarithm of hydraulic conductivity, the flow speed, porosity and the mean hydraulic gradient. The method quantifies particle motion in spatially variable flow fields through a stochastic model for equidistantly sampled particle speeds along streamlines. Thus, it propagates solute particles at constant space increments whose duration is obtained from a Markov chain representation for the particle speed. The model is predictive because it can be parameterized by transport independent medium and flow characteristics. This approach has been used for the upscaling and prediction of solute transport from the pore to Darcy scale, and from the Darcy to the field scale in two- and three-dimensional porous and fractured media [11, 41–48]. In the following, we detail the model, its assumptions, and parameterization.

### A. Stochastic advective motion

We choose a Lagrangian framework [4] and focus on the advective motion of tracer particles, which constitute the tracer plume. The temporal variation patters of particle velocities are in general rather complex. They are intermittent because their evolution is governed by a broad distribution of times scales, which are determined by the flow speeds and characteristic length scales imprinted in the medium structure [40, 49]. The complexity of intermittent temporal series of particle velocities can be removed by adopting an equidistant point of view. Therefore, unlike classical Lagrangian approaches we do not consider particle motion isochronically, but equidistantly along streamlines. This means, we quantify motion through transitions over constant space increments instead of constant time increments. It has been shown for the pore and the Darcy scale [40, 42, 48, 50] that equidistant series of particle velocities can be modeled as Markov chains.

Thus, advective particle motion is quantified by the following stochastic evolution equations for the longitudinal particle position $x(s)$ and the advective travel time $t_a(s)$ [41, 49],

$$\frac{dx(s)}{ds} = \chi^{-1}, \qquad \frac{dt_a(s)}{ds} = \frac{1}{v_\ell(s)} \tag{1}$$

where $s$ is the distance along streamline, and $v_\ell(s) > 0$ the particle speed, this means the magnitude of the equidistant particle velocity. The distance $s$ along the streamline is in general larger than the linear travel distance $x$ in the mean flow direction. They are projected onto each other through the advective tortuosity $\chi$, which is given by the ratio of the average flow speed $\langle q \rangle$ and the average velocity component $\langle q_1 \rangle$ in mean flow direction, $\chi = \langle q \rangle / \langle q_1 \rangle$ [41]. The angular brackets denote suitably chosen averages, here spatial and ensemble average. The particle speed $v_\ell(s)$ describes an ergodic and stationary Markov process characterized by the steady state distribution $p_v(v)$. The latter is a Lagrangian quantity, which, however, can be related to the distribution of Eulerian flow speed $p_e(v)$ via the flux-weighting relation [41, 49]

$$p_v(v) = \frac{v p_e(v)}{\langle v \rangle}, \tag{2}$$

Note that $v_\ell(s)$ evolves as a function of distance $s$ along a streamline, while in classical Lagrangian methods [4], particle speeds evolve with travel time. This difference explains the flux-weighting relationship (2) as discussed in detail in Dentz *et al.* [49] and Hakoun *et al.* [40].

The Eulerian velocity $\mathbf{v}(\mathbf{x})$ is given in terms of the Darcy flux $\mathbf{q}(\mathbf{x})$, porosity $\phi$, and the retardation coefficient $\theta$, which accounts for linear equilibrium sorption. We assume that both porosity and retardation are constant. The Darcy flux satisfies

$$\mathbf{q}(\mathbf{x}) = -K(\mathbf{x}) \nabla h(\mathbf{x}), \qquad \nabla \cdot \mathbf{q}(\mathbf{x}) = 0, \tag{3}$$

where $K(\mathbf{x})$ is hydraulic conductivity and $h(\mathbf{x})$ hydraulic head. The flow problem (3) is solved numerically for a unit mean hydraulic gradient aligned with the coordinate axis in one-direction, and a unit geometric mean conductivity $K_g = 1$, see Appendix A. The Eulerian velocity $\mathbf{v}(\mathbf{x})$ is given in terms of the resulting Darcy velocity $\mathbf{q}(\mathbf{x})$ as

$$\mathbf{v}(\mathbf{x}) = v_0 \mathbf{q}(\mathbf{x}) \qquad v_0 = K_g J / \phi\theta \tag{4}$$

where $J$ is the magnitude of the mean hydraulic gradient. The velocity $v_0$ and the correlation length $\ell_c$ define the characteristic time $\tau_v = \ell_c / v_0$. Note that changes in $v_0$ affect transport only through a rescaling of time. The Eulerian speed is $v(\mathbf{x}) = |\mathbf{v}(\mathbf{x})|$, and its distribution is, as introduced above, denoted by $p_e(v)$. The magnitude of $\mathbf{q}(\mathbf{x})$ is denoted by $q(\mathbf{x})$. Based on (4), the Eulerian speed distribution is given in terms of the distribution $p_q(q)$ of $q(\mathbf{x})$ as

$$p_e(v) = p_q(v/v_0)/v_0. \tag{5}$$

In this work, hydraulic conductivity is represented by a three-dimensional lognormally distributed spatial random field. The horizontal correlation length is $\ell_h = 5\ell_v$ and the variance of the logarithm $f(\mathbf{x}) = \ln[K(\mathbf{x})]$ of hydraulic conductivity is set to $\sigma_f^2 = 5.9$ reflecting the conductivity statistics estimated for the MADE site [51]. We find $\langle q_1 \rangle = 3.04$ and $\langle q \rangle = 3.5$. This implies that the effective conductivity is $K_e = 3.04 K_g$, and the advective tortuosity $\chi = 1.15$. Figure 1 shows the distributions of $f(\mathbf{x}) = \ln[K(\mathbf{x})]$ and $\nu(\mathbf{x}) = \ln[q(\mathbf{x})]$. The distribution $p_\nu(\nu)$ of $\nu(\mathbf{x})$ can be modeled by the skewed Gaussian distribution

$$p_\nu(\nu) = \frac{\exp\left[-\frac{(\nu-m)^2}{2\sigma_\nu^2}\right]}{\sqrt{2\pi\sigma_\nu^2}} \Phi[\alpha(\nu - m)/\sqrt{\sigma_\nu^2}], \tag{6}$$

where $\Phi(x)$ is the cumulative unit Gaussian distribution. The parameters in Figure 1 are $\sigma_\nu^2 = \sigma_f^2 = 5.9$, $\alpha = 1.29$ and $m = 1.47$.

Regarding the propagation of the particle speeds $v_\ell(s)$ from their initial values $v_0 = v_\ell(0)$, the key feature is the spatial persistence of speeds, which is characteristic for transport in steady flow fields [19, 22, 42, 49]. This spatial persistence is at the origin of intermittent Lagrangian flow properties in porous media found both at the pore and Darcy scales [40, 45, 50, 52]. Thus velocity transitions have been modeled, for example through independent sampling after fixed persistence lengths [13], Bernoulli processes [11, 40, 49], and by empirical velocity transition matrices [42, 43]. In this work, we consider the evolution of the normal score $w(s)$ of $v_\ell(s)$, which is given by

$$w = \Phi^{-1}[P_v(v)], \qquad v = P_v^{-1}[\Phi(w)]. \tag{7}$$

The cumulative probability of $p_v(v)$ is denoted by $P_v(v)$, its inverse by $P_v^{-1}(v)$. The Doob theorem states that the only process that is both Markovian and Gaussian is the Orrnstein-Uhlenbeck process [53, 54]. For this reason, we model the evolution of $w(s)$ through the Ornstein-Uhlenbeck process [54]

$$\frac{dw(s)}{ds} = -\ell_c^{-1} w(s) + \sqrt{2\ell_c^{-1}}\eta(s), \tag{8}$$

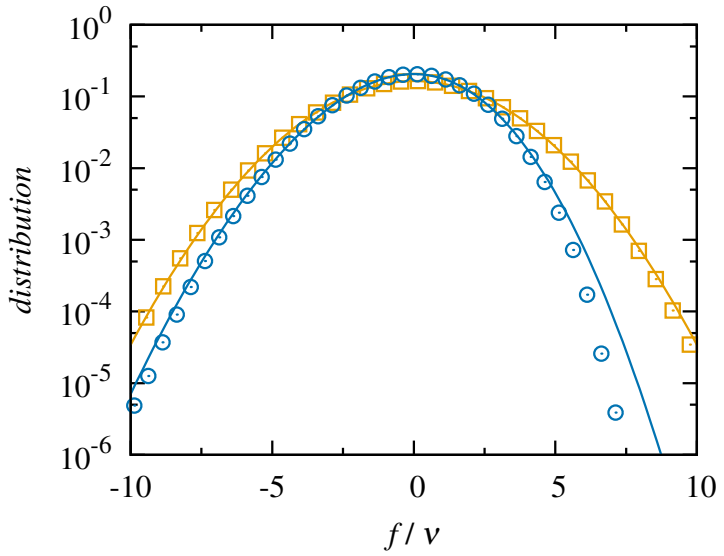


Figure 1. (Squares) empirical distribution of $f(\mathbf{x})$. The solid orange line denotes the normal distribution with zero mean and variance $\sigma_f^2 = 5.9$. (Circles) empirical distribution of the logarithm $\nu(\mathbf{x})$ of the flow speed. The blue solid line denotes the skewed normal distribution (6).

where $\eta(s)$ is a Gaussian white noise characterized by 0 mean and correlation $\langle \eta(s)\eta(s')\rangle = \delta(s-s')$. The steady state distribution of $w(s)$ is the unit Gaussian. The initial values $w(0)$ of the normal scores are obtained from $v(0)$ through the Smirnov transform (7). The initial velocity distribution is denoted by $p_0(v)$. The correlation length $\ell_c$ of the normal score $w(s)$ is set equal to $\ell_c = 8\ell_h/3$ [22, 40, 41]. This approach has been used and verified for the prediction of equidistant Lagrangian velocity series and intermittent transport characteristics in pore and Darcy scale heterogeneous porous media [40, 41, 45, 50].

Equations (1) together with the evolution equation for $v_\ell(s)$, describe the propagation of the particle position $x(s)$ and velocity $v_\ell(s)$ from the initial values $x(0)$, and $v(0)$, which are distributed according to $\rho(x)$, and $p_0(v)$. The initial value of time is $t(0) = 0$. The projected streamwise concentration profile $c(x,t)$ of the mobile, this means non-adsorbed solute in this framework is obtained by

$$c(x,t) = \theta^{-1} \left\langle \delta\left[x - s(t)/\chi\right]\right\rangle, \tag{9}$$

where $s(t) = \max[s|t_a(s) \leq t]$. The angular brackets denote here the average over all particles. The TDRW approach is intrinsically mass conservative. Thus its density describes the total, this means adsorbed and non-adsorbed concentrations, which is the reason why the non-adsorbed concentration is obtained from the total density through division by $\theta$ as given in (9).

This stochastic TDRW approach is parameterized by the Eulerian speed distribution, advective tortuosity and the correlation length $\ell_c$. These quantities are constrained by the geometric mean conductivity, the variance and correlation lengths of the logarithm of hydraulic conductivity, the mean hydraulic gradient, and porosity, without non-physical fitting parameters. This means the model is parameterized in terms of geostatistical and hydraulic characteristics that can be determined by transport independent measurements, and is in this sense predictive. In addition, the approach can account for linear equilibrium sorption.

In the following, we use this upscaled transport model to predict the longitudinal plume evolution of the MADE-1 and MADE-2 experiments. Its numerical implementation is detailed in Appendix B.

## III. PREDICTION OF DISPERSION AT THE MADE SITE

We use the upscaled transport model presented in the previous section for the prediction of the streamwise tracer profiles of the MADE-1 and MADE-2 experiments [7, 55]. For the MADE-1 experiment, we consider six snapshots of the longitudinal bromide concentration profiles [7, 39]. For the MADE-2 experiment, we consider two snapshots of the longitudinal tritium profiles [34, 55]. In the following, we first discuss the model parameters for the MADE site, and then report on the prediction of the longitudinal concentration profiles for the MADE-1 and MADE-2 experiments.

| Parameter | $\sigma_f^2$ | $K_g$ [m/s] | $\ell_h$ [m] | $\ell_v$ [m] | J [-] | $\phi$ | $\theta$ [Br] | $\theta$ [$^3$H] |
|---|---|---|---|---|---|---|---|---|
| Value | 5.9 | $5.5 \times 10^{-6}$ | 9.1 | 1.8 | $3.6 \times 10^{-3}$ | 0.31 | 1.2 | 1 |

Table I. Geostatistical, and hydraulic data for the MADE site, as well as retardation coefficients for the bromide and tritium tracers of the MADE-1 and MADE-2 experiment according to Bohling *et al.* [51], Boggs *et al.* [12], Boggs and Adams [56] and Harvey and Gorelick [30].

### A. Hydraulic and transport parameters for the MADE site

We consider purely advective transport, which is a reasonable assumption given that the Péclet number at the MADE site is around $10^3$ [39]. In order to parameterize the model, we rely on the description of the experimental conditions in Boggs *et al.* [12] and Adams and Gelhar [7] and the geostatistical characterization of the hydraulic conductivity field given in Bohling *et al.* [51]. Thus, the medium porosity, and the magnitude of the mean hydraulic gradient are set equal to $\phi = 0.31$, $J = 3.6 \times 10^{-3}$ [7, 12, 39]. Bohling *et al.* [51] estimate for the variance of the logarithm of conductivity $\sigma_f^2 = 5.9$ and for the horizontal and vertical correlation lengths $\ell_h = 9.1$ m and $\ell_v = 1.8$ m. For the geometric mean conductivity these authors obtain the average value of $K_g = 6.7 \times 10^{-6}$ m/s. The upper and lower limits of the 95% confidence interval around this value are $K_g = 10^5$ m/s and $K_g = 4.3 \times 10^{-6}$ m/s. Here we use the value $K_g = 5.5 \times 10^{-6}$ m/s because it provides a better prediction of the observed peak concentration values. The model predictions for $K_g = 6.7 \times 10^{-6}$ m/s and a discussion of the evolution of the peak values are given in Appendix D.

The values for the predictions of the longitudinal concentration profiles shown below are summarized in Table I. The characteristic velocity $v_0$ is given by $v_0 = 6.39 \times 10^{-8}\theta^{-1}$ m/s and the average transport velocity by $\langle v_1 \rangle = K_e J/\phi\theta = 1.94 \times 10^{-7}\theta^{-1}$ m/s. We use for the prediction of both the MADE-1 and MADE-2 data the same medium and hydraulic parameters. Boggs and Adams [56] found from column experiments the values $\theta = 1.2$ and $\theta = 1$ for the retardation coefficients of bromide and tritium. The retardation coefficient accounts for the fact that only the mobile, non-adsorbed solute is measured [30, 56], and in this sense accounts for a measurement bias.

The parameter values specified above determine the propagator of the upscaled transport model. In order to predict the plume evolution, we need both the propagator, and the initial conditions, this means here, the initial particle positions, and initial particle speed distribution. As described in Boggs *et al.* [12] and Stauffer *et al.* [57], in both experiments tracer was injected into five 5.2-cm-diameter injection wells separated by 1 m in a linear array perpendicular to the mean flow direction. In both experiments, tracer was injected in about 10 m$^3$ of groundwater for the duration of 48.5 hours. Thus, while the initial distribution of the tracer plume was indeed spatially extended in the transverse and longitudinal direction, we use here for simplicity a pointlike initial particle distribution, localized at the origin at $x = 0$,

$$\rho(x) = \delta(x). \tag{10}$$

Regarding the initial velocity distribution $p_0(v)$, we note that Boggs *et al.* [12] and Fiori *et al.* [39] pointed out that more mass entered in the high than in the low conductivity zones, which implies that the initial mass distribution is approximately flux-weighted. In order to set the initial velocity distribution $p_0(v)$, we assume that the initial plume extension is large enough to be considered ergodic [39]. Under this assumption, $p_0(v)$ can be set equal to $p_v(v)$ given by Eq. (2). Note that the model can be conditioned on velocity data within the initial plume if detailed information is available. Below we use this approach to model and predict the longitudinal concentration profiles of the MADE-1 and MADE-2 experiments.

### B. Longitudinal concentration profiles

The experimental concentration profiles for the MADE-1 experiment are based on the bromide tracer data from Adams and Gelhar [7] normalized to the initial mass as given in Fiori *et al.* [39]. The concentration profiles for the tritium tracer at the MADE-2 experiment are obtained from Salamon *et al.* [34].

Figures 2 and 3 show the experimental data and the model predictions. As explained in Adams and Gelhar [7] and Salamon *et al.* [34], the displayed data was obtained by interpolation of concentration values between sampling wells, vertical and transverse integration of the resulting concentration field, and longitudinal averaging over a window of $\Delta x = 10$ m [7, 34]. The bin centers are located at $x_i = -15$ m $+ i10$ m with $i = 0, \ldots, 19$. The injection position is at $x = 0$. Concentration values are normalized by the initial mass. The longitudinal concentration distribution is shown at six snapshots at times $t = 49, 126, 202, 279, 370$ and 503 days for MADE-1 and at $t = 27$ and 328 d for MADE-2. The tracer distributions predicted from the upscaled model are presented in the same way. Appendix C

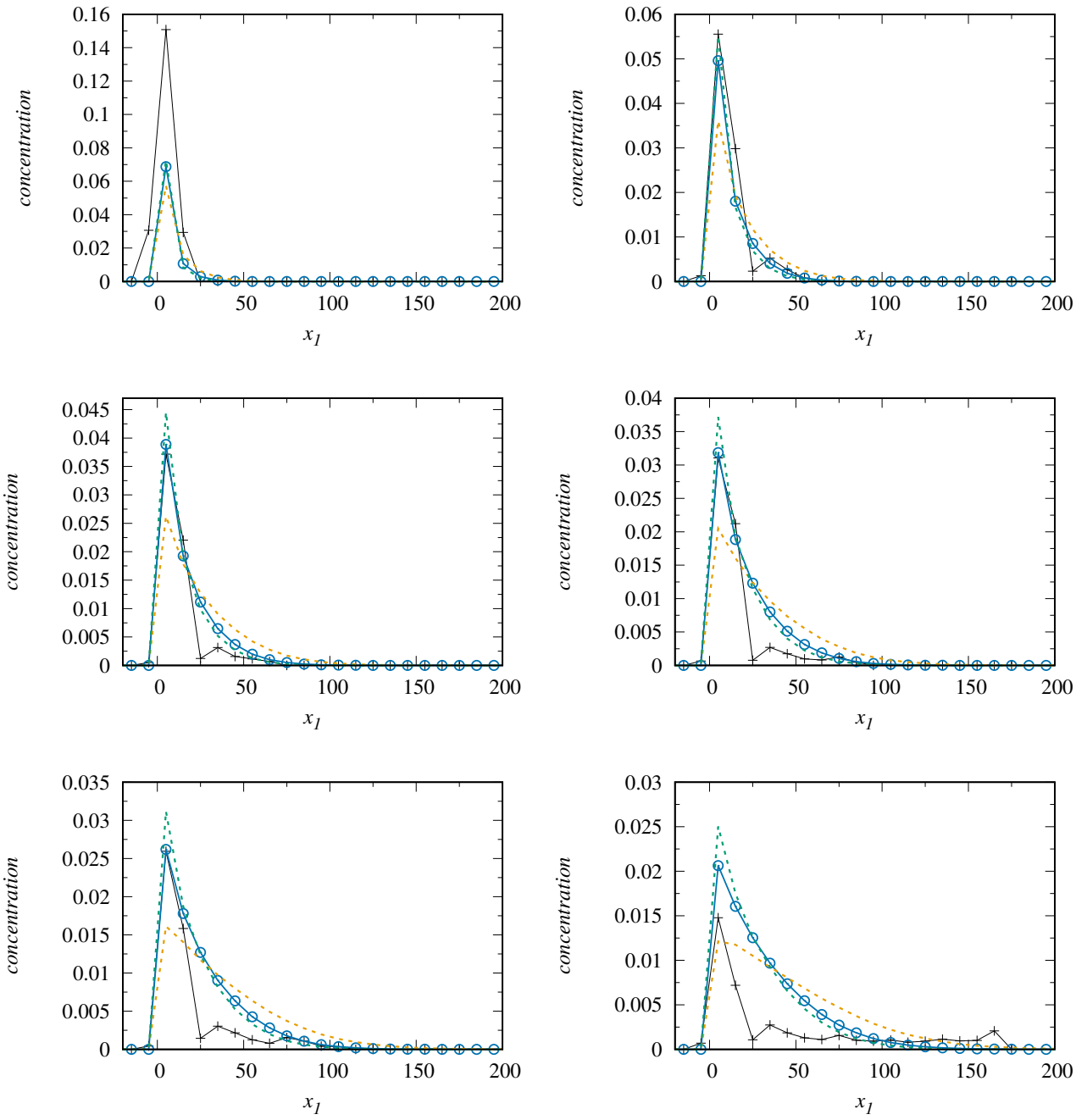


Figure 2. Concentration profiles from (crosses) the MADE-1 data and (circles) the upscaled model for an averaging window of $\Delta x = 10$ m at times (top left to bottom right) $t = 49$ d, 126 d, 202 d, 279 d, 370 d and 503 d using a pointlike initial distribution. The dashed lines denote the predictions for the values of (green) $K_g = 4.3 \times 10^{-6}$ m/s and (orange) $K_g = 10^5$ m/s at the lower and upper limits of the 95 % confidence interval of $K_g$.

provides the tracer distributions with an averaging window of $\Delta x = 10^{-1}$ m for MADE-1. We refer to the latter as the fine scale model data.

We first note that the experimental data does not integrate to 1. In fact the mass under the longitudinal profiles for the MADE-1 data integrates to $2.06, 0.99, 0.68, 0.62, 0.54$ and $0.43$ for the six snapshots at increasing time [7, 39] and to 1.52 and 0.77 at $t = 27$ d and 328 d for the MADE-2 snapshots [57]. The explanation of this apparent mass loss has been a matter of debate in the literature. Several authors [30, 34, 56, 58] attribute the overestimation of mass at early, and underestimation at late times to a measurement bias due to preferential sampling from high conductivity

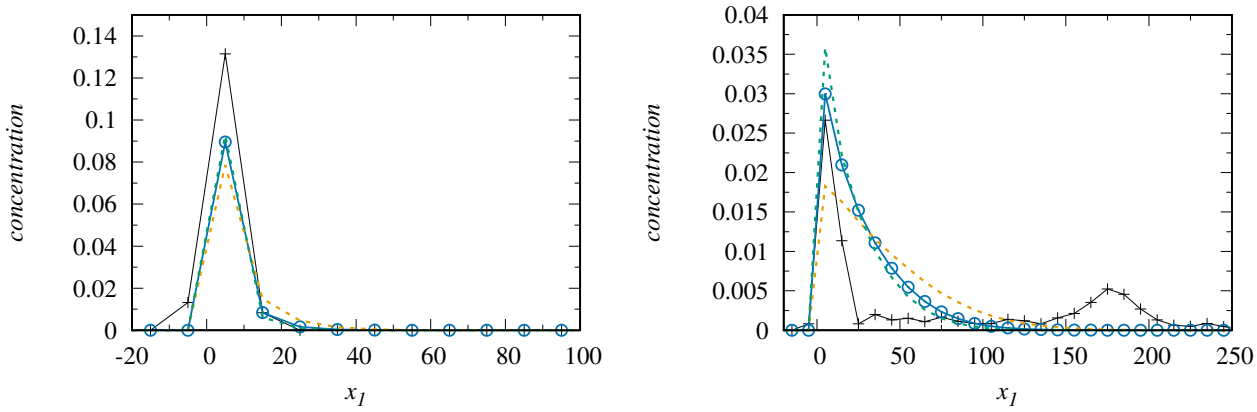


Figure 3. Analogous to Figure 2 for the concentration profiles of the MADE-2 experiments at $t = 27$ d and 328 d.

regions and mass transfer into immobile regions. In fact, the analysis of core samples two years after the MADE-1 experiment by Boggs and Adams [56] indicate that a substantial amount of mass may have been transferred and stored in immobile zones. Other authors [7, 39] debate that the mass loss could be attributed to a decreasing density of sampling points at distances larger than 20 m downstream from the injection region. This view is supported by the fact that more mass loss is observed for the bromide plume in the MADE-1 [7] than for the tritium plume in the MADE-2 experiment [57], for which the density of sampling wells was increased.

The tracer distribution in the upscaled TDRW model is by default normalized to $1/\theta$, which, as outlined above accounts for a possible sampling bias due to adsorption. Figures 2 and 3 display model predictions for $K_g = 5.5 \times 10^{-6}$ m/s, and $K_g = 10^5$ m/s, and $K_g = 4.3 \times 10^{-6}$ m/s at the upper and lower limits of the confidence interval. The model predicts the overall shape of the observed tracer distributions, the slow moving peak, and the development of a forward tail with increasing time. For increasing $K_g$, the velocity spectrum is shifted to higher values. Thus, the peak height and peak retention decrease, the forward tail increases. While the value of $K_g = 5.5 \times 10^{-6}$ m/s provides the best prediction for the peak concentrations, all $K_g$ values give qualitatively the same non-Gaussian tracer profiles. This shows the robustness of the salient non-Gaussian transport features predicted by the TDRW approach. The upscaled model accounts for retention of tracer mass in the injection region through persistent low initial flow speeds. The forward tailing is accounted for through the presence of high initial flow velocities in combination with fast tracer motion through particle transitions into spatially persistent fast velocity channels.

The predicted mass in the tails at 126 d to 370 days (MADE-1) is generally higher for $x > 25$ m than in the experimental data, while the reach is relatively well reproduced, see also the corresponding logarithmic plots in Appendix C. As mentioned above, this discrepancy between model and data may be attributed to a decreasing density of sampling points more than 20 m downstream from the injection [7, 39]. The last snapshots at $t = 503$ d for the MADE-1 and $t = 328$ d for the MADE-2 experiments show farther reaching forward tails with secondary peaks, which are not captured by the TDRW model. These features in the data may be attributed to a sampling bias.

## IV. CONCLUSIONS

We have presented a Lagrangian stochastic model for transport in heterogeneous aquifers that is parameterized in terms of the statistical characteristics of hydraulic conductivity and Eulerian flow speed. The approach is based on a Markov processes for equidistant particle speed, whose steady state distribution is given by the flux-weighted flow speed distribution. The latter is derived from the distribution of the Eulerian flow speed, which is obtained from standardized numerical flow simulations, this means, for unit gradient of hydraulic head and unit geometric mean conductivity. The model is parameterized by the mean, variance and correlation lengths of the logarithm of hydraulic conductivity, advective tortuosity, porosity. These model inputs are transport independent, this means they can be assessed by medium and flow characterization. These features yield a predictive upscaled approach for advective tracer transport in heterogeneous aquifers. Like other stochastic models, this approach relies on the ergodicity of the underlying medium heterogeneity. The model furthermore accounts for linear instantaneous equilibrium sorption.

We use this upscaled model to assess and predict the evolution of the bromide tracer plume of the MADE-1 and the tritium plume of the MADE-2 experiments, which are characterized by strongly non-Gaussian shapes. Relatively

low conductivity in the source zone leads to slow peak movement of only a few meters over the duration of the experiments, while part of the tracer moves fast, which gives rise to a pronounced forward tail. The slow moving peak is captured by the upscaled model through the low velocity end in the distribution of initial particle speeds. The developing forward tail is quantified by tracer propagation due to spatially persistent broadly distributed particle speeds. The speed distributions are determined by the medium and Eulerian flow statistics. As mentioned above all model parameters are obtained from transport independent measurements, without recourse to fitting parameters. We find that the purely advective upscaled model provides a robust estimate of the evolution of the overall plume shape. Our results indicate that the large scale transport features of the MADE-1 and MADE-2 plumes may be explained by flow heterogeneity due to spatial variability in hydraulic conductivity. The proposed upscaled model is predictive, transferable to different solutes and hydraulic conditions, and seems to capture the salient heterogeneity mechanisms, and their impact on large scale transport.

## ACKNOWLEDGMENTS

We thank Daniel Fernandez-Garcia for sharing the data for the two concentration snapshots of the MADE-2 experiment, and Alraune Zech and Aldo Fiori for sharing the MADE-1 data with us. The authors acknowledge the financial support of the European Research Council through the project MHetScale (Grant agreement No. 617511), and the Spanish Ministry of Science and Innovation through a Severo Ochoa project (No. CEX2018-000794-S), and the project HydroPore (PID2019-106887GB-C31). Juan Hidalgo acknowledges the support of the Spanish Ministry of Science and Innovation through a Ramón y Cajal fellowship. The experimental data was published originally in Adams and Gelhar [7] and reproduced in Fiori *et al.* [39], from where the data in the present work is obtained. The TDRW model data is availabe at http://dx.doi.org/10.20350/digitalCSIC/12667.

[1] J. Bear, *Dynamics of Fuids in Porous Media* (American Elsevier, New York, 1972).
[2] L. W. Gelhar and C. L. Axness, Water Resour. Res. **19**, 161 (1983).
[3] G. Dagan, J. Fluid Mech. **145**, 151 (1984).
[4] G. Dagan, *Flow and transport in porous formations* (Springer, New York, 1989).
[5] L. W. Gelhar, *Stochastic subsurface hydrology* (Prentice Hall, 1993).
[6] Y. Rubin, *Applied stochastic hydrogeology* (Oxford University Press, New York, 2003).
[7] E. E. Adams and L. W. Gelhar, Water Resour. Res. **28**, 3293 (1992).
[8] M. Levy and B. Berkowitz, Journal of Contaminant Hydrology **64**, 203 (2003).
[9] R. Haggerty, S. A. McKenna, and L. C. Meigs, Water Resour. Res. **36**, 3467 (2000).
[10] C. Zheng, M. Bianchi, and S. M. Gorelick, Groundwater **49**, 649 (2011).
[11] P. K. Kang, T. Le Borgne, M. Dentz, O. Bour, and R. Juanes, Water Resour. Res. **51**, 940 (2015).
[12] J. M. Boggs, S. C. Young, L. M. Beard, L. W. Gelhar, K. R. Rehfeldt, and E. E. Adams, Water Resour. Res. **28**, 3281 (1992).
[13] B. Berkowitz, A. Cortis, M. Dentz, and H. Scher, Rev. Geophys. **44**, RG2003 (2006).
[14] S. P. Neuman and D. M. Tartakovsky, Adv. Water Resour. **32**, 670 (2008).
[15] M. Dentz, T. Le Borgne, A. Englert, and B. Bijeljic, J. Cont. Hydrol. **120-121**, 1 (2011).
[16] B. Noetinger, D. Roubinet, A. Russian, T. Le Borgne, F. Delay, M. Dentz, J.-R. De Dreuzy, and P. Gouze, Transport in Porous Media , 1 (2016).
[17] R. Haggerty and S. M. Gorelick, Water Resour. Res. **31**, 2383 (1995).
[18] J. Carrera, X. Sánchez-Vila, I. Benet, A. Medina, G. Galarza, and J. Guimerà, Hydrogeology Journal **6**, 178 (1998).
[19] B. Berkowitz and H. Scher, Phys. Rev. Lett. **79**, 4038 (1997).
[20] D. A. Benson, S. W. Wheatcraft, and M. M. Meerschaert, Water Resources Research **36**, 1403 (2000).
[21] J. H. Cushman and T. R. Ginn, Water Resour. Res. **36**, 3763 (2000).
[22] V. Cvetkovic, H. Cheng, and X.-H. Wen, Water Resour. Res. **32**, 1671 (1996).
[23] A. Fiori, I. Jankovic, G. Dagan, and V. Cvetkovic, Water Resour. Res. **43**, W09407 (2007).
[24] J. Cushman and T. Ginn, Transp. Porous Media **13**, 123 (1993).
[25] S. P. Neuman, Water Resour. Res **29**, 633 (1993).
[26] B. Berkowitz and H. Scher, Phys. Rev. E **57**, 5858 (1998).
[27] D. A. Benson, R. Schumer, M. M. Meerschaert, and S. W. Wheatcraft, Transport in porous media **42**, 211 (2001).
[28] R. Schumer, D. A. Benson, M. M. Meerschaert, and B. Bauemer, Water Resour Res **39(10)**, 1296 (2003).
[29] Y. Zhang and D. A. Benson, Geophysical Research Letters **35**, n/a (2008).
[30] C. Harvey and S. M. Gorelick, Water Resources Research **36**, 637 (2000).
[31] C. E. Feehley, C. Zheng, and F. J. Molz, Water Resources Research **36**, 2501 (2000).
[32] J. Guan, F. J. Molz, Q. Zhou, H. H. Liu, and C. Zheng, Water Resources Research **44** (2008), 10.1029/2007wr006120.

[33] H. C. Barlebo, M. C. Hill, and D. Rosbjerg, Water Resour. Res. **40**, W04211 (2004).
[34] P. Salamon, D. Fernàndez-Garcia, and J. J. Gómez-Hernández, Water Resour. Res. **43**, W08404 (2007).
[35] M. Dogan, R. L. Van Dam, G. Liu, M. M. Meerschaert, J. J. Butler Jr., G. C. Bohling, D. A. Benson, and D. W. Hyndman, Geophys. Res. Lett. **41**, 7560 (2016).
[36] V. Cvetkovic, A. Fiori, and G. Dagan, Water Resources Research **50**, 5759 (2014).
[37] Y. Edery, A. Guadagnini, H. Scher, and B. Berkowitz, Water Resour Res **50 (2)**, 1490 (2014).
[38] A. Tyukhova, M. Dentz, W. Kinzelbach, and M. Willmann, Physical Review Fluids **1**, 074002 (2016).
[39] A. Fiori, G. Dagan, I. Jankovic, and A. Zarlenga, Water Resources Research **49**, 2497 (2013).
[40] V. Hakoun, A. Comolli, and M. Dentz, Water Resour. Res. **55**, 10.1029/2018WR023810 (2019).
[41] A. Comolli, V. Hakoun, and M. Dentz, Water Resources Research **55**, 8197 (2019).
[42] T. Le Borgne, M. Dentz, and J. Carrera, Phys. Rev. E **78**, 041110 (2008).
[43] P. K. Kang, M. Dentz, T. Le Borgne, and R. Juanes, Phys. Rev. Lett. **107**, 180602 (2011).
[44] P. K. Kang, P. de Anna, J. Nunes, B. Bijeljic, M. J. Blunt, and R. Juanes, Geophys. Res. Lett. **41 (17)**, 6184 (2014).
[45] V. L. Morales, M. Dentz, M. Willmann, and M. Holzner, Geophysical Research Letters **44**, 9361 (2017).
[46] P. K. Kang, M. Dentz, T. Le Borgne, S. Lee, and R. Juanes, Adv. Water Resour. (2017), 10.1016/j.advwatres.2017.03.024.
[47] A. Puyguiraud, P. Gouze, and M. Dentz, Transport in Porous Media **128**, 837 (2019).
[48] J. D. Hyman, M. Dentz, A. Hagberg, and P. K. Kang, Journal of Geophysical Research: Solid Earth (2019), 10.1029/2018jb016553.
[49] M. Dentz, P. K. Kang, A. Comolli, T. Le Borgne, and D. R. Lester, Physical Review Fluids **1**, 074004 (2016).
[50] A. Puyguiraud, P. Gouze, and M. Dentz, Water Resources Research **55**, 1196 (2019).
[51] G. C. Bohling, G. Liu, P. Dietrich, and J. J. Butler, Water Resources Research **52**, 8970 (2016).
[52] P. de Anna, T. Le Borgne, M. Dentz, A. M. Tartakovsky, D. Bolster, and P. Davy, Phys. Rev. Lett. **110**, 184502 (2013).
[53] J. L. Doob, Annals of Mathematics , 351 (1942).
[54] C. W. Gardiner, Applied Optics **25**, 3145 (1986).
[55] J. Boggs, L. Beard, W. Waldrop, T. Stauffer, W. MacIntyre, and C. Antworth, *Transport of tritium and four organic compounds during a natural-gradient experiment (MADE-2)*, Tech. Rep. (Electric Power Research Inst., Palo Alto, CA (United States); Tennessee Valley Authority, Norris, TN (United States). Engineering Lab.; Air Force Engineering and Services Center, Tyndall AFB, FL (United States), 1993).
[56] J. M. Boggs and E. E. Adams, Water Resources Research **28**, 3325 (1992).
[57] T. B. Stauffer, C. P. Antworth, R. G. Young, W. G. MacIntyre, and J. Boggs, *Degradation of aromatic hydrocarbons in an aquifer during a field experiment demonstrating the feasibility of remediation by natural attenuation*, Tech. Rep. (TENNESSEE VALLEY AUTHORITY NORRIS, 1994).
[58] F. J. Molz, C. Zheng, S. M. Gorelick, and C. F. Harvey, Water Resources Research **42** (2006), 10.1029/2005wr004265.
[59] F. Ruan and D. McLaughlin, Advances in Water Resources **21**, 385 (1998).

## Appendix A: Flow solution

The hydraulic conductivity fields are generated using the spectral method of Ruan and McLaughlin [59] with an exponential covariance function. The flow problem (3) is solved numerically using a two-point flux finite volume method in 40 realizations of $f(\mathbf{x})$ whose spatial mean and variance are within a 0.05 tolerance interval around the target values of 0 and 5.9. The flow domains have the dimensions $20\ell_h$ in the direction of the mean gradient, $10\ell_h$ in the transverse horizontal direction, and $10\ell_v$ in vertical direction. The resolution is $2^8 \times 2^7 \times 2^5$ voxels.

## Appendix B: Numerical model implementation

In the following, we outline the basic steps of the numerical implementation of the stochastic time domain random walk model combined with mass transfer between mobile and immobile regions. First, we note that the steady state Eulerian velocity distribution $p_e(v)$ is given by the distribution show in Figure 1. The distribution $p_v(v)$ of particle speeds is obtained according to (2) by flux-weighting.

*Step 1: Initialization* Initial particle velocities $v(0)$ are sampled from $p_v(v)$, particle positions $x(0)$ are chosen from the initial particle distribution $\rho(x)$, which here is $\rho(x) = \delta(x)$.

*Step 2: Propagation of normal scores* The initial velocities $v(0)$ are then converted to the initial values $w(0)$ of the normal scores using the map (7). The normal scores $w(s)$ are propagated from their initial values $w(0)$ according to the Ornstein-Uhlenbeck process (8), which is discretized by using an Euler scheme. This gives

$$w(s + \Delta s) = w(s)\left(1 - \ell_c^{-1}\Delta s\right) + \sqrt{2\ell_c^{-1}\Delta s}\zeta(s), \tag{B1}$$

where $\zeta(s)$ denotes a Gaussian random variable with zero mean and unit variance. The discretization $\Delta s$ is chosen much smaller than $\ell_c$. Here we set $\Delta s = 10^{-1}$ m.

*Step 3: Propagation of particle position and time* The particle positions are incremented at each random walk step by $\Delta s/\chi$, the particle times by $\Delta s/v_\ell(s)$,

$$x(s+\Delta s) = x(s) + \frac{\Delta s}{\chi}, \qquad t_a(s+\Delta s) = t_a(s) + \tau_a(s), \qquad \tau_a(s) = \frac{\Delta s}{v_\ell(s)}. \tag{B2}$$

The current particle speed $v_\ell(s)$ is obtained according to Eq. (7).

Steps 2 and 3 are repeated until the maximum simulation time is reached. Particle positions are recorded at steps $s$ if $t(s) \leq t_i$ and $t(s+\Delta s) > t_i$ with $t_i$ the desired observation times.

## Appendix C: Longitudinal concentration profiles,

Figure 4 shows the longitudinal concentration profiles from the MADE-1 data, and the model prediction in coarse and fine resolution for $\theta = 1.2$. The comparison shows that the averaging window of $\Delta x = 10$ m introduces an artificial broadening of the peak due to oversmoothing, while the tail concentrations are nearly identical. With increasing time, as the peak width increases due to hydrodynamic dispersion, the differences between the coarse and fine scale models decrease.

Figure 5 shows the same data as in Figure 2 plotted logarithmically. The tail contains in general more mass than the experimental data, but reproduces relatively well the overall tendency except for the 503 d snapshot at which mass is recovered at larger downstream distances than predicted by the model.

## Appendix D: Predictions for different values of $K_g$ and peak concentrations

Figure 6 compares the model predictions for the MADE-1 data with $\theta = 1.2$ based on the estimated average value of $K_g = 4.3 \times 10^{-6}$ m/s, and the values at the upper and lower limits of the 95% confidence interval. $K_g = 6.7 \times 10^{-6}$ m/s and $K_g = 10^{-5}$ m/s. For all $K_g$ values the model predicts the main plume features of peak localization and forward tail discussed in the main text. The model predictions based on $K_g = 5.5 \times 10^{-6}$ m/s shown in the main text provide slightly better estimates for the concentration peak values at $t \leq 370$ d than the ones using the mean $K_g = 6.7 \times 10^{-6}$ m/s.

The concentration peak is localized at all snapshots at $x = 5$ m, which indicates that it does not move beyond the averaging window between $x = 0$ m and 10 m. This is supported by the fine scale prediction. The upscaled model predicts peak heights and widths that are qualitatively and quantitatively similar to the experimental observations. The peak concentrations from the experimental data, and the corresponding model predictions are displayed in Figure 8. The upscaled model predicts the overall decay of the peak concentration. The decay behavior in the localized peak is in fact a measure for the residence time in the injection region. The mass $m_0(t)$ remaining in the region between 0 m and 10 m is equal to the probability that the residence time $\tau_0$ of a particle is larger than $t$,

$$m_0(t) = \int_t^\infty dt' \psi_0(t'), \tag{D1}$$

where $\psi_0(t)$ denotes the residence time distribution. As long as the mass in the injection region of size $\Delta x$ is larger than the mass in all other bins, the peak concentration is equal to $c_0(t) = m_0(t)/\Delta x$. Figure 8 shows the evolution of $c_0(t)$ from experimental data and model predictions obtained from the upscaled model. In order to highlight the impact of the value of geometric conductivity, we also plot the decay of the maximum concentration for the values $K_g = 6.7 \times 10^{-6}$ m/s and the values at the upper and lower limits of the 95% confidence interval, $K_g = 10^{-5}$ m/s and $K_g = 4.3 \times 10^{-6}$ m/s, as well as the corresponding distributions of $\nu = \ln(v)$. The former underestimates the observed maximum concentrations because, as shown in the right panel of Figure 8 the distribution of $\nu$ is characterized by higher values than for the lower $K_g$. This feature together with the persistence represented by the correlation length $\ell_c$ of particle velocities leads to a relatively fast tracer release from the injection domain compared to the other values for $K_g$. The value of $K_g = 4.3 \times 10^{-6}$ m/s overestimates the maximum concentration because of strong tracer retention at the injection region due to low initial speeds. Nevertheless, the predictions using these $K_g$ values provide robust prediction of the salient non-Gaussian behaviors of the tracer profiles.

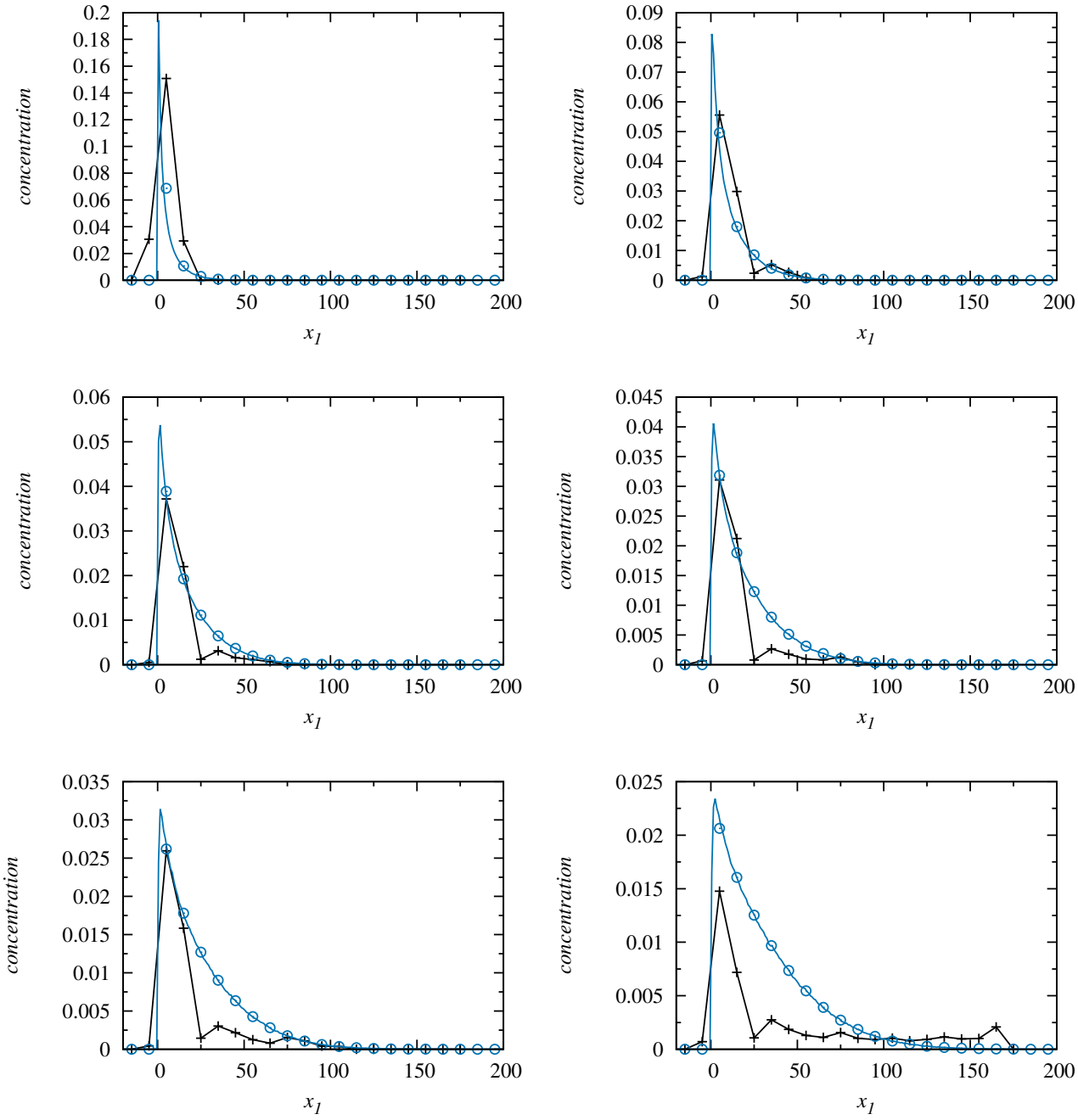


Figure 4. Concentration profiles from (crosses) the MADE data and the upscaled model for an averaging window of (circles) $\Delta x = 10$ m and (solid blue line) $\Delta x = 10^{-1}$ m at times (top left to bottom right) $t = 49$ d, 126 d, 202 d, 279 d, 370 d and 503 d.

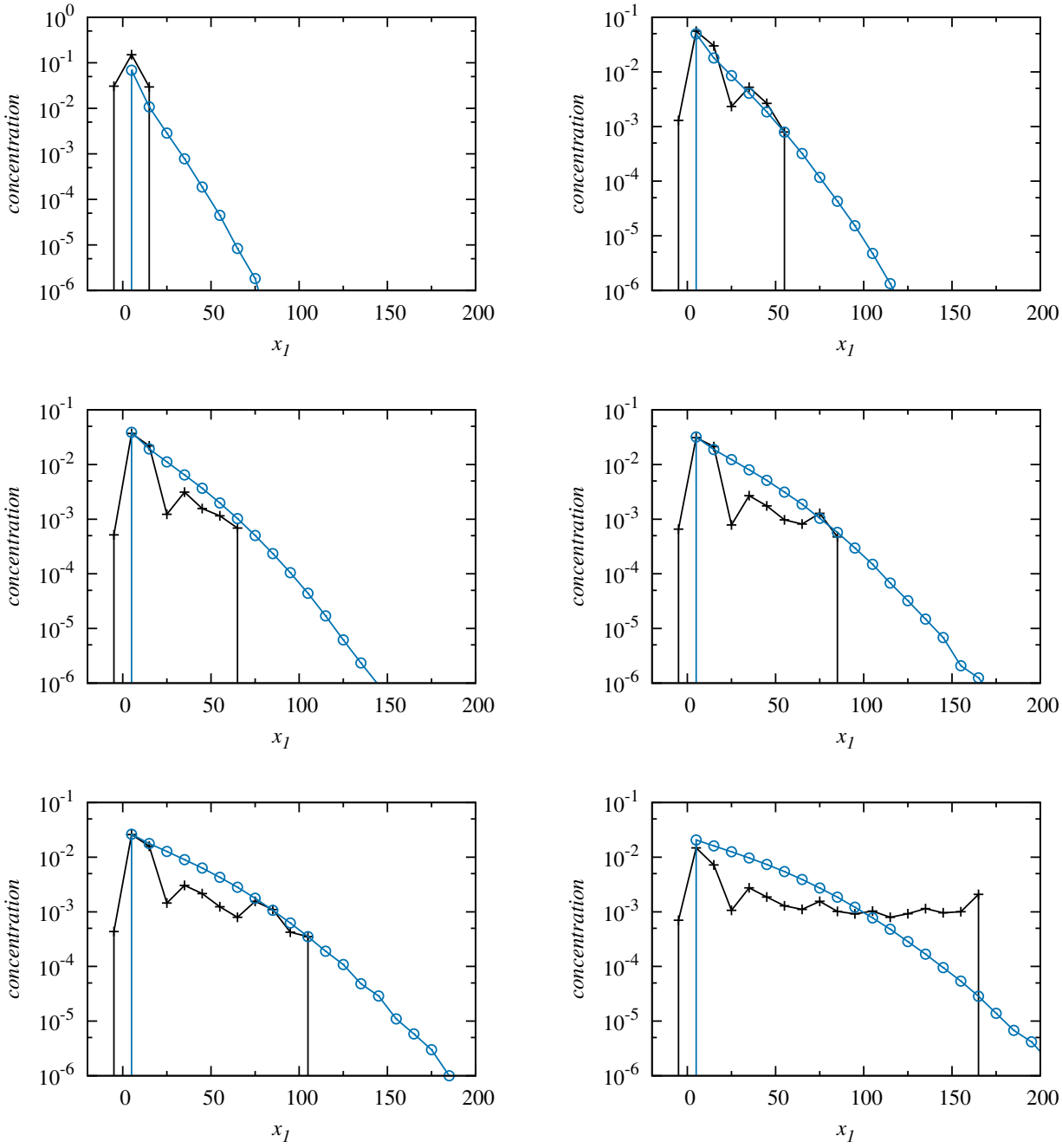


Figure 5. Same concentration data as in 2 plotted logarithmically on the concentration axis.

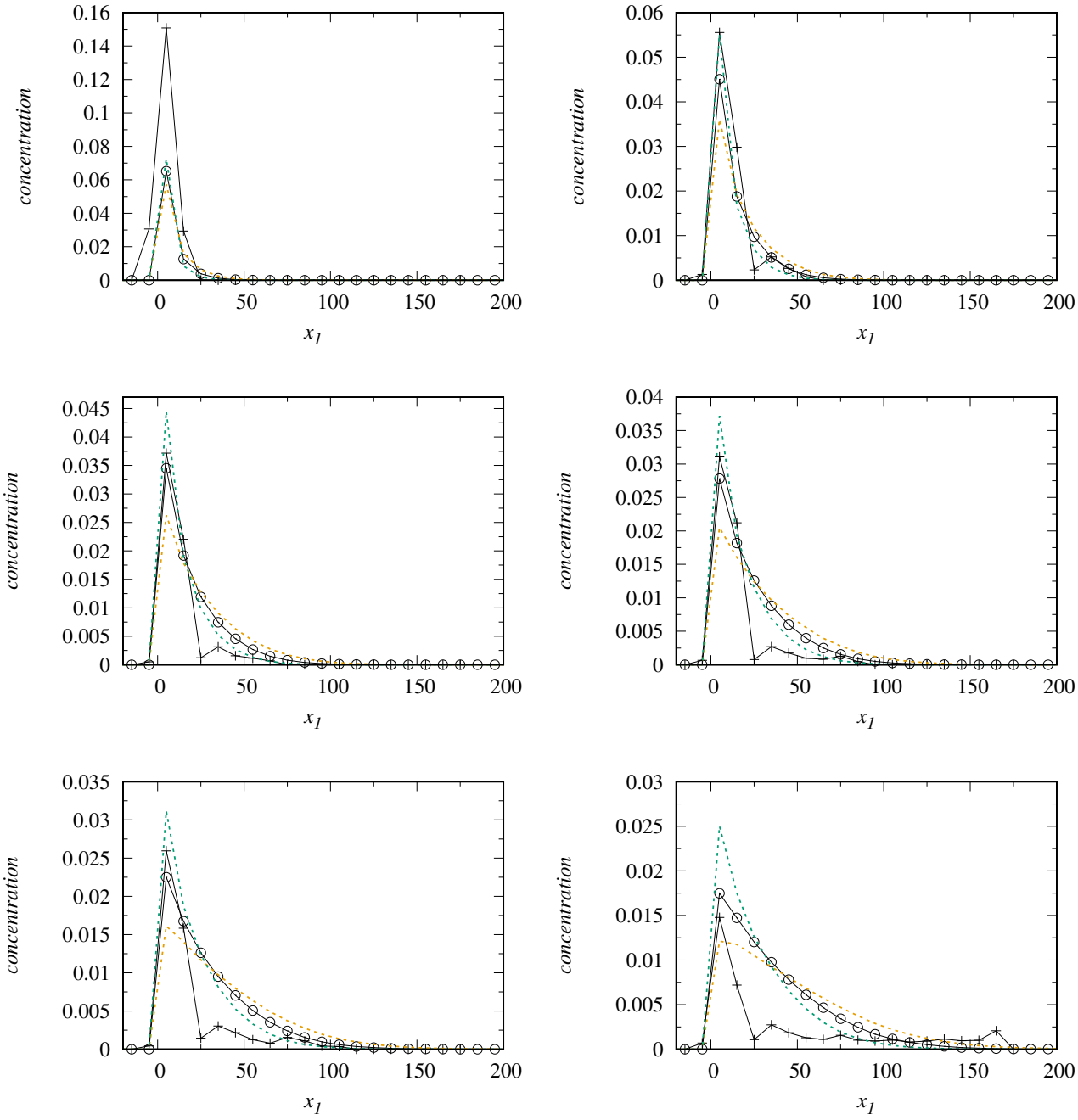


Figure 6. Concentration profiles from (crosses) the MADE-1 data and (circles) the upscaled model using $K_g = 6.7 \times 10^{-6}$ m/s for an averaging window of $\Delta x = 10$ m at times (top left to bottom right) $t = 49$ d, 126 d, 202 d, 279 d, 370 d and 503 d using a pointlike initial distribution. The dashed lines denote the predictions for (green) $K_g = 4.3 \times 10^{-6}$ m/s, (orange) $K_g = 10^{-5}$ m/s.

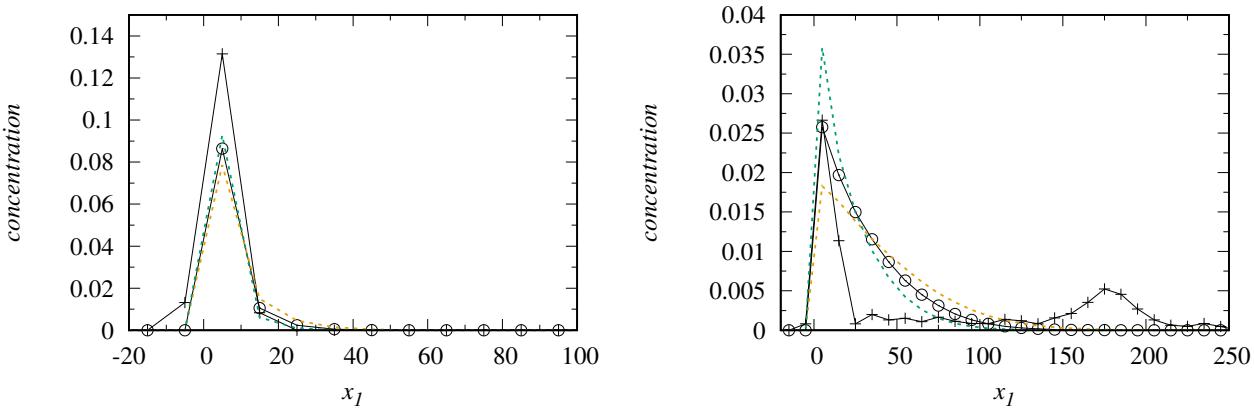


Figure 7. Analogous to Figure 6 for the MADE-2 data at $t = 27$ d, and 328 d.

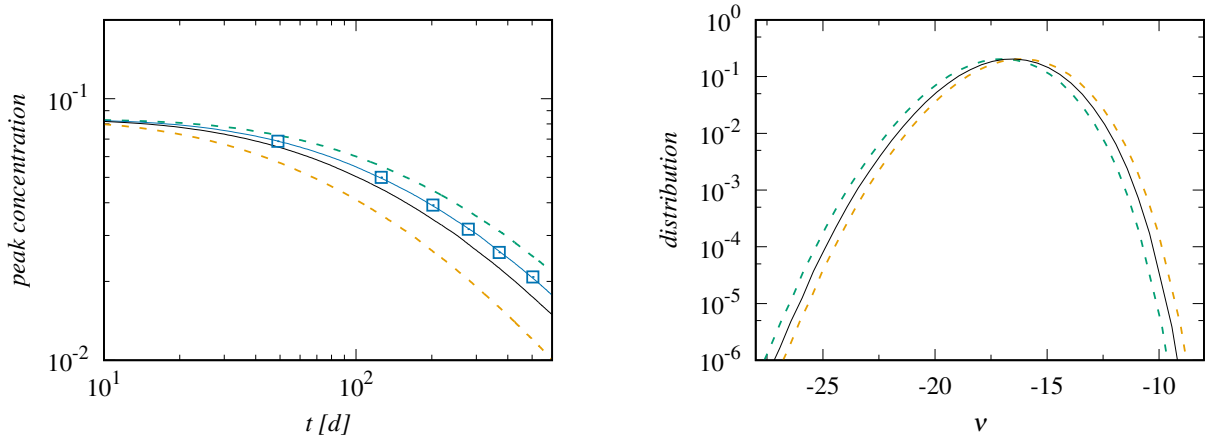


Figure 8. (Left panel) Maximum concentrations versus time from the (black crosses) MADE-1 data, and (blue squares) the prediction from the upscaled model with $\Delta x = 10$ m. The dashed lines denote the cumulative distribution of residence times (D1) obtained from the upscaled model for (green) $K_g = 4.3 \times 10^{-6}$ m/s, (orange) $K_g = 10^{-5}$ m/s. The black solid line denotes the prediction for $K_g = 6.7 \times 10^{-6}$ m/s. (Right panel) Distributions of the corresponding $\nu = \ln(v)$.